Insights from reactive transport models of basalt and water experiments

Dale Emet Altar*, Eylem Kaya and Sadiq J. Zarrouk

Department of Engineering Science, University of Auckland, Private Bag 92019, Auckland, New Zealand

*dalt507@aucklanduni.ac.nz

Keywords: *TOUGHREACT, reactive transport, numerical model, supercritical, basalt*

ABSTRACT

TOUGHREACT™ was used to create reactive transport models to match the results of detailed laboratory simulations of the interactions between tholeiitic basalt and distilled de-oxygenated water. The fluid-rock interaction experiments were carried out under two sets of conditions, one under subcritical conditions (350 °C and 490 bar) and the second under supercritical conditions (400 °C and 500 bar). The experimental environments are associated with seafloor spreading centres and mid-ocean ridges.

Methodologies were developed for building the reactive transport models, focusing primarily on the reaction thermodynamics and kinetics parameters at high temperature and pressure conditions. Initial geochemical assumptions made for the models were also validated and updated during model calibration.

Based on the model, precipitation rates deviated significantly from the combination of the estimated kinetic parameters and mineral surface area estimates, while there is an agreement in terms of dissolution rates. In concurrence with experimental results, mineral solid solutions dissolved stoichiometrically in the model except for bytownite, whose albite component was preferentially dissolved, resulting in its alteration to anorthite. The volumes of basalt glass in the samples were also higher than experimental estimates based on the models. Sulfide inclusions in the glass were added to the model assumptions to explain the observed sulfate and sulfide concentrations while the glass dissolved. The potassium concentration trends in the effluents also necessitated the inclusion of K-feldspar in the model system.

1. INTRODUCTION

Reactive transport models are valuable tools in geothermal management as they aid in understanding the hydrologic, thermal and geochemical processes that occur in the reservoir, including their interactions. Notable applications include the works of Clearwater et al. (2015), Castillo Ruiz et al. (2021), and Xu et al. (2004). Geochemical processes in the presence of carbon dioxide were the focus of Altar and Kaya (2020), Audigane et al. (2005), Erol et al. (2022), Knauss et al. (2005) and Xu et al. (2005, 2007), while Seol and Lee (2007), André et al. (2008), Kovac et al. (2006) and Williams et al. (2010) studied non-traditional geothermal developments.

Numerical studies based on experimental simulations allow the verification of reaction rates at the experiment temperature and pressure conditions to supplement the currently available data for mineral reactions. Surface area normalised reaction rate constants calculated from model results can be used for other reactive systems, including fractured media. Models based on experiments with variable flow rates can also be used to isolate the effect of the mass transfer coefficient on the overall reaction rate. These experiments may also be used to validate chemical equilibrium conditions calculated from empirical equations of state. The findings may then be used to refine reservoir modelling efforts and contribute to the analysis methodology for subsurface mineral alterations (dissolution and deposition), geothermal fluid chemistry evolution, dissolved gas content, and reservoir porosity and permeability distributions.

Another knowledge gap that this work can address is in reactive environments under supercritical water conditions where experimental data are limited. The results can supplement modelling capabilities for future work on supercritical geothermal resources.

This study focuses on reactive transport models of experiments conducted by Passarella (2021), which simulated the reaction between basalt and distilled water at subcritical conditions (350 °C and 490 bar) and supercritical conditions (400 °C and 500 bar). Fresh, unreacted tholeiitic basalt from the Elvarpahraun flow of the Svartsengi volcanic system in the Reykjanes Peninsula, Iceland (Peate et al., 2009) was used in the experiment. Their study aimed to understand the system of hydrothermal reactions and the resulting secondary mineralogy and textures associated with seafloor spreading centres and mid-ocean ridges (Passarella et al., 2015, 2017). Their data set provided a suitable basis for this modelling study, with sufficient information to constrain the reaction processes and kinetics. The model, in turn, gives insight into the mineral reaction rates under the experimental conditions, the chronology of the reaction processes, as well as other characteristics of the basalt.

2. METHODOLOGY AND MODEL SET-UP

TOUGHREACT™ (Xu et al., 2014), a comprehensive non-isothermal multi-component reactive fluid flow and geochemical transport simulator based on TOUGH2™, was used to set up the reactive transport models. The EOS1 module was used to estimate the thermodynamic fluid properties for pure water (in its liquid, vapour, and two-phase states), with typical applications to hydrothermal problems. Additional work on the model grid creation, model automation and graphing was done with PyTOUGH (Croucher, 2011, 2015; Wellmann et al., 2012, 2014). SUPCRTBL (Zimmer et al., 2016) was used to estimate the necessary thermodynamic data for all chemical species and reactions in the model.

The model reactor is cylindrical, with a height of 151.6 mm and a radius of 6.35 mm. The total volume simulation domain was divided into 1000 computational blocks; 50 layers and 20 radial blocks per layer (Figure 1). Smaller grid blocks were placed near the reactor entry to capture localised alteration effects, especially since experimental observations indicate that the highest degree of alteration occurred adjacent to the reactor entry.

ISSN 2703-4275

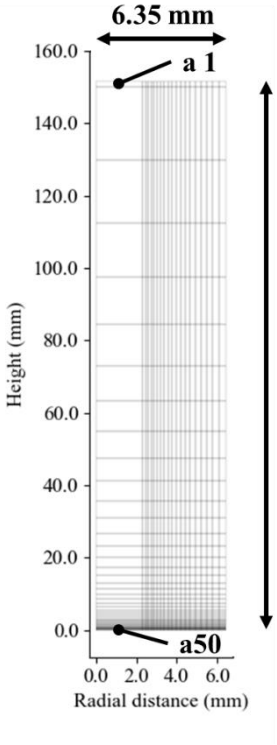

Figure 1: Slice view of the reactor model grid. The fluid injection block 'a50' and the fluid extraction block 'a 1' are indicated (Altar et al., 2022, with permission).

The initial porosities of the crushed rock samples used in the experiments were 0.522 for the subcritical experiment and 0.53 for the supercritical experiment. Block permeabilities in the model were set to 6.5×10^{-14} m^2 (65 mD) in all directions. Fluid injection was assigned to block 'a50', the centre block at the bottom of the reactor corresponding to the physical inlet (Figure 1). Extraction was set to block 'a 1', the centre block at the top corresponding to the reactor outlet.

Both experiments were run at room temperature (~20 °C) and experimental pressure for the first six days. After this initial period, reactor temperatures were raised to the respective target conditions and maintained until the end of the simulations. Fluid flow in both experiments was set at 1 ml hr^{-1} (2.8×10^{-7} kg s^{-1}) for the majority of the runs except for the last six days in the subcritical experiment and the last four days in the supercritical experiment, wherein the flow rates were decreased to 0.5 ml hr^{-1} (1.4×10^{-7} kg s^{-1}). The model parameters were set to reflect these conditions. These resulted in three regions of different pressure, temperature and flow conditions for both experiments, illustrated for the supercritical investigation in Figure 2.

For each model, the initial and boundary fluids have the same component concentrations, adopted from the blank fluid concentrations measured at the time of each experiment. The chemical components used in the models were Na^+, K^+, Ca^{2+}, Mg^{2+}, Fe^{2+}, Al^{3+}, Cl^-, SO_4^{2-}, $H_4SiO_{4,aq}$, $Ti(OH)_{4,aq}$, H_2S_{aq} and pH.

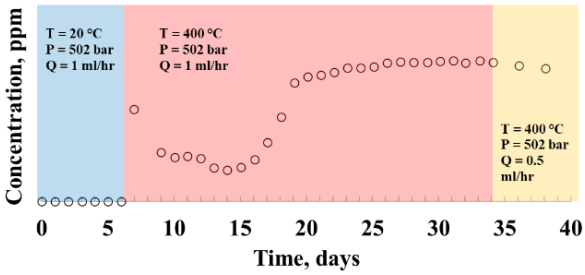

Figure 2: Plot of sodium concentration data for the supercritical experiment, showing the periods of varying experimental conditions.

The mineral composition of the basalt samples was analysed before and after the experiment via electron microprobe analysis (EMPA), scanning electron microscopy with electron dispersive spectroscopic analysis (SEM-EDS) and quantitative X-ray diffraction analysis (XRD). The estimated abundances of each primary mineral for this study are shown in Table 1. Secondary minerals identified after the experiments were also included in the model with initial volume fractions of 0.0%.

Table 1: Mineralogy and initial volume fractions used in the models for the basalt samples.

	Mineral	% Vol
Primary	Bytownite	62.4%
	Clinopyroxene	29.3%
	Olivine	1.9%
	Titanomagnetite	3.8%
	Glass	2.6%
Secondary	Anorthite	0%
	Chlorite	0%
	Celadonite	0%
	Titanite	0%
	Grossular	0%
	Wollastonite	0%
	Magnetite	0%

For mineral kinetics, TOUGHREACT™ implements the generalised Transition State Theory (TST) Rate Law (Eq. 1) based on the work by Lasaga (1984; 1998; 2018). The reaction rate of the nth mineral in the system (r_n, mol kg^{-1} s^{-1}) is a function of the rate constant (k_n), surface area (A_n), the activities of species to which rates are dependent (Πa_i^{mi}), chemical affinity (Q/K_n), where Q and K_n are the activity product and equilibrium constant for the reaction, respectively, and the exponents η and θ which describe the relationship of the rate to chemical affinity. Both exponents η and θ were assigned initial values of 1.0 for this study. The value of k_n is temperature-dependent following the Arrhenius equation (Eq. 2). It is expressed as a function of the rate constant at 25°C ($k_{25,n}$), the activation energy (Ea, kJ mol^{-1}), the ideal gas constant (R, kJ mol^{-1} K^{-1}) and the reaction temperature (T, K).

ISSN 2703-4275

$$r_n = \pm k_n A_n \prod_{i=1}^{N} {a_i}^{m_i} \left[1 - \left(\frac{Q}{K_n}\right)^{\theta}\right]^{\eta} \quad (1)$$

$$k_n = k_{25,n} \exp\left[\frac{-Ea}{R}\left(\frac{1}{T} - \frac{1}{298.15}\right)\right] \quad (2)$$

The initial k_{25}, Ea and power term (m_i) parameters were adopted from Palandri & Kharaka (2004) for the dissolution kinetics of most minerals. For minerals not explicitly covered in their data set, the parameters from associated minerals were used, primarily if they belong to the same solid solution series. pH-dependent rate terms were included in the model. For basaltic glass, the dissolution rate law and parameters by Gislason and Oelkers (2003) and Oelkers and Gislason (2001) were selected for the model, which included the dependence of the dissolution rate on both solution pH and aluminium concentration.

The initial precipitation rate constants (k_{prec}) were estimated as the ratio of the dissolution rate constant (k_{diss}) and the equilibrium constant (K_{eq}) for the reaction following Horiuti (1957). The relationship is shown in Eq. (3), in which the variable $\upsilon(r)$ is a function of the number of reaction steps, assumed to have a value of one for simplicity.

$$k_{prec} = \frac{k_{diss}}{{K_{eq}}^{1/\upsilon(r)}} \quad (3)$$

Most of the solid solution minerals in the system (augite, olivine, titanomagnetite, celadonite and chlorite) were treated as individual minerals that reacted stoichiometrically to align with experimental observations. The only exception to this treatment was bytownite which dissolved non-stoichiometrically, leaving behind anorthite. The kinetics of anorthite and albite were decoupled to improve parameter control during modelling, a practice that was also done by Sonnenthal et al. (2005) and Sonnenthal and Spycher (2001).

SUPCRTBL (Zimmer et al., 2016) was used for the thermodynamic database. SUPCRTBL is an extension of the SUPCRT92 program (Johnson et al., 1992), incorporating updated properties and additional data sets. Thermodynamic data for the reactions of all aqueous species and end-member minerals were calculated for temperatures between 0°C and 400°C at a constant pressure of 490 bar. The redox couple selected was H_2S_{aq}/SO_4^{2-}.

For solid solution minerals, equilibrium constants were calculated from the values of their respective end members. The solid-solution aqueous-solution equilibrium conditions were formulated following the stoichiometric saturation model of Thorstenson and Plummer (1977). The relationship between K_{SS} (solid solution equilibrium constant) and the equilibrium constants of each end-member mineral (K_i) in a solid solution is given in Eq. (4). For simplicity, it was assumed that the solid solutions were ideal such that end-member activities are equal to their respective molar fractions ($a_i = x_i$). The equilibrium constant for glass was estimated in a similar procedure but was based on the equilibrium constants of its component oxides following the work of Paul (1977), Techer et al. (2001) and Leturcq et al. (1999).

$$K_{SS} = \prod_{i=1}^{n} {K_i}^{x_i} {a_i}^{x_i} \quad (4)$$

The models were calibrated to match the experimental fluid chemistry and mineral alteration by controlling mineral reaction kinetics. This was done by manipulating the activation energies while maintaining k_{25} at the original values. The combination of both parameters provided the best estimate for the rate constant in the reactive system that would fit the chemistry and mineral data. In case the fluid flow rate through the reactor had an observable effect on the reaction rates, the impact is likewise accounted for through the activation energy, which changes the effective rate constant of the reaction involved.

The input mineral surface areas (A^0_m, $m^2/m^3_{mineral}$) and mineral radius (r, m) were estimated based on the average sample particle radius and individual mineral volume fractions for all primary minerals. Starting mineral surface area values were based on the work by White and Peterson (1990), where they defined a relationship between r and physical surface area (PSA, $m^2/m^3_{mineral}$) for non-spherical particles, shown in Eq. (5). They also reported differences between the physical surface area and reactive surface area. The estimated physical surface areas were reduced by three magnitudes to get the values for A^0_m.

$$\log(PSA) = -0.99[\log(200r)] - 2.38 \quad (5)$$

For secondary minerals, the same method was used to estimate A^0_m while values for r were set to 0, essentially setting their RSAs to constant values. Generally, both A^0_m and r were fixed throughout the modelled periods. However, allowances were made for revising the A^0_m values as needed to account for RSA evolution behaviour that diverged from the internally implemented relationship between reactive surface area and particle diameters in TOUGHREACT™.

It is recognised that the combination of the rate parameters and the RSA inputs correspond to the actual reaction rates of each mineral in the experiment. Therefore, some errors in the RSA estimates may also introduce errors in the final kinetic parameters used during calibration.

3. MODEL PERFORMANCE

Model performance was assessed based on both effluent chemistry and mineralogical observations. For effluent chemistry, the model was calibrated primarily relative to silica, sodium, potassium, iron, calcium, sulfate, sulfide and chloride, while the secondary bases of calibration include aluminium, magnesium and pH. The effluent chemistry results are presented in Figure 3 for the components Na^+, K^+, Ca^{2+}, H_4SiO_4, Al^{3+} and H_2S.

For both models, mineral reaction rates at room temperature were negligible, and the modelled concentrations did not deviate from the values for the unreacted fluid. This agrees well with the measurements made during the first six days of both experiments, as seen in Figure 3. Despite the unsaturated state of water relative to all the primary minerals in the basalt, dissolution was not kinetically favoured at low temperatures.

Reaction kinetics improved significantly after reaction temperatures were raised. The early parts of the high-temperature periods (between day six and day 20) were characterised by the rapid dissolution of glass, correlated by Passarella (2021) to the measured concentrations of silica, sulfate, hydrogen sulfide and chloride in the effluents. Their concentrations increased significantly after the temperature increase, followed by a declining trend. This was observed

ISSN 2703-4275

in both experiments and was likewise reflected in the behaviour of both models. By the end of the declining trends at around day 20 in both experiments, glass was completely dissolved across the reactor in both models. Thus chloride, sulfate and hydrogen sulfide concentrations dropped to zero. After the loss of glass, dissolved silica came primarily from plagioclase dissolution and minor contributions from olivine.

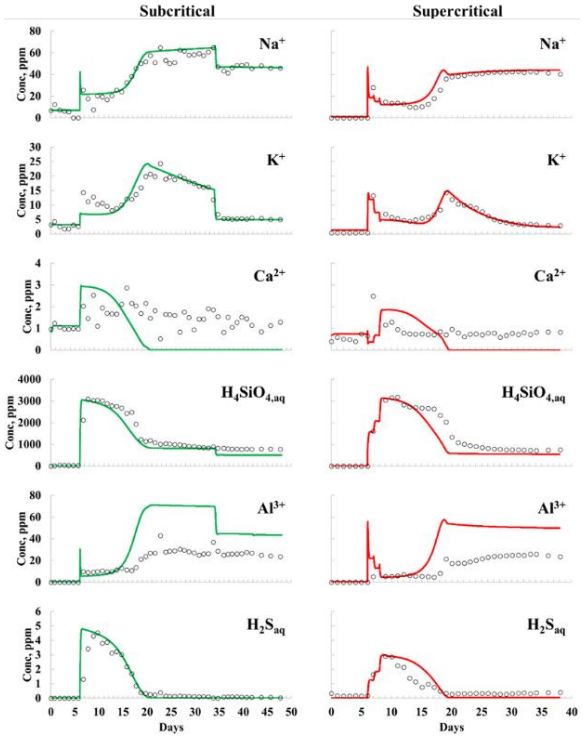

Figure 3: Model results (solid green and red lines) plotted against experimental concentration data (empty circles) for Na^+, K^+, Ca^{2+}, H_4SiO_4, Al^{3+} and H_2S.

Based on the model results, glass dissolution was found to slow down or inhibit the dissolution of the other primary minerals as it increases the component concentrations in the fluids. At the same time, celadonite formed from the dissolution products resulting in low concentrations of sodium and potassium in the effluents (compared to the later parts of the experiments) immediately after the temperature increases. Consequently, the loss of glass resulted in the increased dissolution of the other minerals, primarily observed as upward trends in sodium, potassium and aluminium concentrations that coincided with the downward trends for silica, sulfate, sulfide and chloride. The higher concentrations immediately following the loss of glass in the model were due to increased plagioclase dissolution, particularly for sodium and potassium. In the subcritical model, a rapid decrease in sodium and potassium concentrations at around day 34 was observed, modelled as reactive surface area decrease though the physical mechanism for this has not been identified.

As can be seen in Figure 3, the model and experiment data don't match for all chemical components perfectly. For example, significant amounts of calcium were released from glass dissolution. To approximate the calcium effluent concentrations observed during the period of glass dissolution, precipitation rate parameters for sphene, wollastonite and grossular were tuned. Once glass disappeared, the dissolution of anorthite and augite released significantly less calcium into the fluids. The further formation of calcium-containing secondary minerals resulted in near-zero modelled concentrations. For aluminium, the models only corresponded to the experiments for the first eight days after the temperature increase, then deviated as glass disappeared. Despite the values offset in the latter periods, similarities in trends between the models and the experiments were observed. These discrepancies are expected given the various sources of uncertainty in the model. However, there is still a general agreement between the models and the experiment based on the majority of the chemical components.

In terms of mineralogical observations, one of the most notable is the alteration of the plagioclase bytownite to anorthite adjacent to the reactor entry for both experiments. This was modelled as incongruent dissolution of the bytownite, where the albite component dissolved preferentially. The model results are shown in Figure 4. The altered region is more significant in the subcritical model, with a lower final anorthite mole fraction, which agrees with experimental observations.

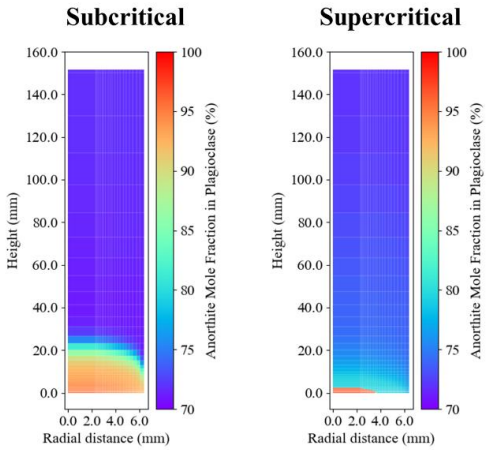

Figure 4: Model results for the alteration of bytownite to anorthite showing the extent of the modelled alteration.

Another notable alteration is the formation of celadonite. In both experiments, it was observed at the reactor exit point but not adjacent to the entry. For the supercritical experiment, it was also observed at points 5-10 mm from the reactor entry. Analysis of the models' intermediate time steps shows that the celadonite's deposition front coincides with the dissolution front for glass. This is shown in Figure 5 for the subcritical model. Olivine, which dissolved across the modelled reactor, also contributed to the formation of celadonite. After the complete dissolution of glass, celadonite that formed close to the reactor entry dissolved.

In both models, augite dissolution only occurred in the first 2 mm from the reactor entry. This agrees with the supercritical experiment, while it was observed even at 5 mm in the subcritical experiment. Titanomagnetite was supersaturated in both models and did not dissolve, in agreement with experimental observations. There is also agreement on chlorite, magnetite, titanite and grossular formation locations.

Overall, the net result of the concurrent mineral dissolution and precipitation processes in the models reduced the total mass. The highest volume losses occurred around the reactor

ISSN 2703-4275

entry, where the maximum dissolution rates also occurred. Subsequently, porosity was modelled to increase across the reactors.

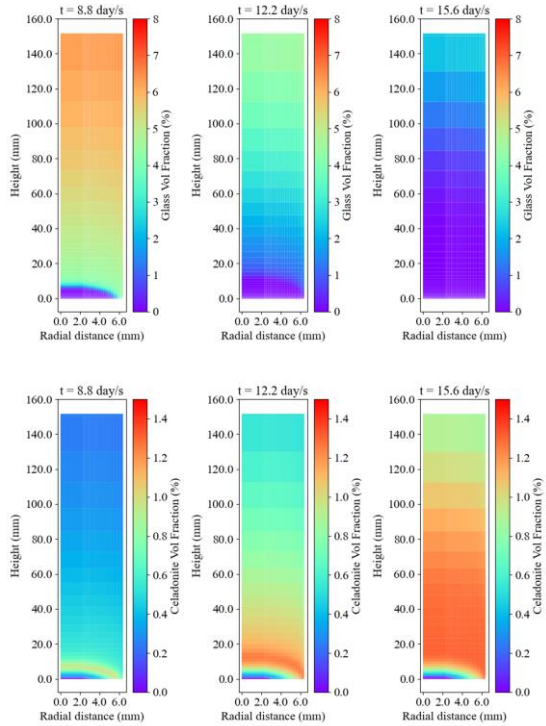

Figure 5: Subcritical model results for glass dissolution (top row) and celadonite deposition (bottom row) over time.

4. INSIGHTS INTO THE BASALT COMPOSITION

The presence and dissolution of glass are significant factors in the geochemical processes that were observed in the experiments. Thus, substantial effort was given to review model assumptions for the glass. The first is the amount in the sample. The initial estimate of 2.5% by weight was based on silica flux analysis on the effluents. The analysis implies that any silica released from glass dissolution remained in solution and that the silica component of the secondary minerals was produced from the other primary minerals. However, while glass remained in the system, it suppressed the dissolution of anorthite, albite, and augite. The effluents were near equilibrium for olivine, resulting in low dissolution rates. Thus, glass was the most likely source of silica in the early parts of the high-temperature period for secondary mineral formation. The modelled basalt's glass content was increased to account for the silica requirement. The resulting estimates based on the models are 7.7% and 7.2% by weight in the subcritical and supercritical experiments.

Sulfur content in the modelled samples (only reported in glass) was also adjusted. Initially, sulfur was modelled to exist purely as sulfide in the glass with the assumption that a fraction was oxidised to sulfate through the reduction of Fe(III), a component of titanomagnetite, to Fe(II), Eq. (6).

$$Fe^{3+} + 0.125H_2S_{aq} + 0.5H_2O \rightleftharpoons Fe^{2+} + 0.125{SO_4}^{2-} + 1.25H^+ \quad (6)$$

However, little to no titanomagnetite dissolved, and the fluids remained Fe(III)-deficient. No other oxidising agents were identified for the reaction system. Consequently, it was assumed that both species are already present in the basalt, where sulfate was taken to comprise 40% by molar basis of the total sulfur content in the glass based on their ratios in the effluents.

Sulfur content in the glass was also increased in the model to match the observed H_2S_{aq} and SO_4^{2-} concentration trends. The original sulfur content based on EMPA was not enough to produce the observed concentrations even with the increased amount of glass. After a review of the experimental data, the higher sulfur concentrations were attributed to the iron sulfide inclusions trapped as immiscible droplets in the glass. These were not considered in the original model assumptions. Empirical adjustments were made to the total sulfur content of the glass in the model to account for the inclusions. The adjusted amounts were within the range of sulfur content for Iceland basalts (Forrest et al., 2017).

K-feldspar was also added to the modelled reaction system. In the original assumptions, potassium was only reported in the glass. In terms of the processes involving potassium, the early proposition was that it was released from glass dissolution, precipitated out in the celadonite, and released back into solution by celadonite dissolution. Though these processes were replicated in the model, the low solubility of celadonite could not produce the observed potassium concentrations after the loss of glass (day 20 onwards). After reviewing the experimental data by Passarella (2021), bytownite (plagioclase) was identified as another source of potassium. Including K-feldspar fractions of 0.7% and 0.35% by molar basis in the bytownite (for the subcritical and supercritical models, respectively) was found sufficient to improve the potassium match. Both are within the range of K-feldspar fraction values in the bytownite samples (0.2% to 0.8%), measured during the experiments via EMPA.

5. REACTION KINETICS

The main parameters for modelling the individual mineral reaction rates are the rate constants, the reactive surface areas and the equilibrium constants (Eq. 1). Under ideal modelling conditions, each of these parameters can be measured and verified separately; however, this is rarely the case. This study used estimates to define the equilibrium constants and mineral surface areas, which have inherent uncertainties. Consequently, the final rate constants used to replicate the experiment results will have uncertainties.

A comparison was made between the rate constants (as a result of Ea adjustments) used in each model and the starting estimates based on published data for dissolution and the calculated values for precipitation. It should be noted that to allow this comparison, the same sets of thermodynamic data and baseline reactive surface area inputs for each mineral were used in both models. The effective rate constants calculated from the original k_{25} values and the adjusted Ea values for both models were plotted against the rate constant curves using the initial model parameters.

Values for selected dissolving minerals are shown in Figure 6. The rate constants take into account the pH-dependent terms. There was general agreement between the rate constants for anorthite, augite, olivine, glass and albite with the published values. Any differences were less than an order of magnitude. For sanidine, the rate constants used in the

ISSN 2703-4275

models were consistently higher by orders of magnitude than the published values.

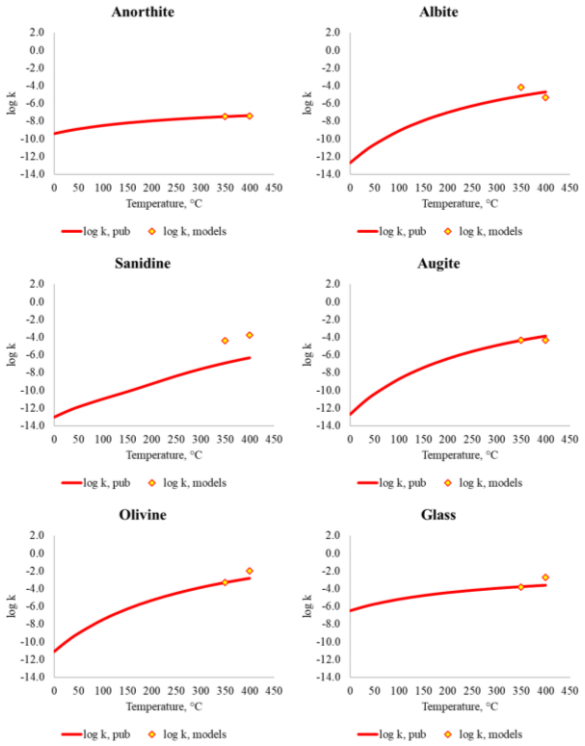

Figure 6: Modelled rate constants for dissolving minerals plotted against published values.

Since the reactive surface area values in the model were three magnitudes less than the physical surface area estimates, overall, the dissolution rates in the experiments align with the observations from other investigators that field-derived reaction rates tend to be orders of magnitude less than values from dissolution rate experiments (Aradóttir et al., 2012; Gislason and Eugster, 1987; White and Brantley, 2003).

A similar comparison was made for the secondary minerals (Figure 7). The model values differed significantly from the initial estimates. Mineral deposition mechanisms in nature are complex, and this deviation from ideality (a base assumption for Eq. 3) could account for the differences.

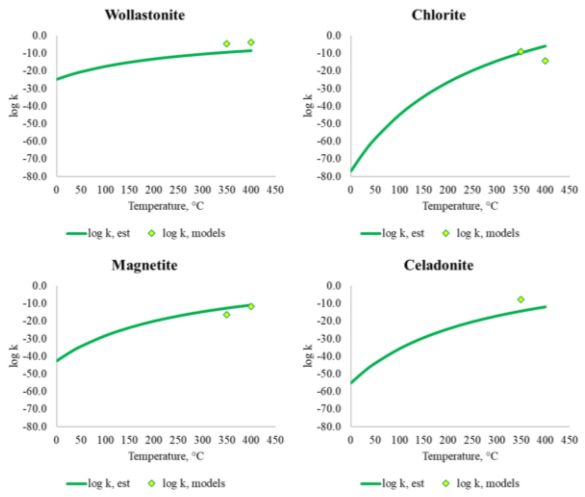

Figure 7: Modelled rate constants for precipitating minerals plotted against published values.

One alternative is to use the dissolution kinetic parameters for the precipitation reactions (Aradóttir et al., 2012; Saldaña et al., 2016; Sonnenthal and Spycher, 2001; Xu et al., 2003, 2004, 2007). Uncertainties are likewise expected with this method of approximation as evidenced by the works of Nagy et al. (1990, 1991), Nagy and Lasaga (1993) and Yang and Steefel (2008) on observed rate differences between dissolution and precipitation.

6. CONCLUSION

The reactive transport models sufficiently captured the mineral reaction kinetics and the interactions of the concurrent dissolution and precipitation processes in the experiment. This is based on the agreement between the experiment results, modelled effluent chemistry, and modelled mineral alteration behaviour.

The estimates and validation of dissolution and precipitation rate constants at 350 °C and 400 °C provide additional information to improve reactive transport modelling capabilities for high-temperature (including supercritical) environments. However, these values are not without uncertainty. Particularly for precipitation, the model values differed by orders of magnitude from theoretically calculated values. In contrast, a minimal divergence of model values from published rate constants was observed for mineral dissolution. However, the use of reduced mineral surface areas indicates that field dissolution rates are orders of magnitude less than values from dissolution rate experiments and should always be considered in reactive transport models.

The thermodynamic data estimates using SUPCRTBL sufficiently represented the geochemical system with a few exceptions. Further improvements may be made by considering non-ideal mixing models for solid solution minerals and building up SUPCRTBL's thermodynamic database as new data becomes available.

Finally, it is good practice to review the mineral and fluid composition and quantity assumptions in models against published and experimental data. Model assumption revisions may be warranted by empirical data and can significantly affect model results.

ACKNOWLEDGEMENTS

This work was supported by the University of Auckland Doctoral Scholarship and the MBIE Research Programme, GNS-MBIE00150 "Geothermal: Next Generation" project, New Zealand.

REFERENCES

Altar, D. E., Kaya, E., Zarrouk, S. J., Passarella, M., & Mountain, B. W.: Numerical geochemical modelling of basalt-water interaction under subcritical conditions. *Geothermics*, *105*, 102520. (2022).

Altar, D. E., Kaya, E.: Numerical Modelling of the Interaction between Geothermal Injectate-Non Condensable Gas Solutions and Greywacke, *International Journal of Greenhouse Gas Control*, *94*. (2020).

André, L., Spycher, N., Xu, T., Pruess, K., & Vuataz, F.: Comparing FRACHEM and TOUGHREACT for reactive transport modeling of brine-rock interactions in enhanced geothermal systems (EGS). Paper

presented at the *31st Workshop on Geothermal Reservoir Engineering*, Stanford University, Stanford, California. (2008).

Aradóttir, E. S. P., Sonnenthal, E. L., Björnsson, G., & Jónsson, H.: Multidimensional reactive transport modeling of CO2 mineral sequestration in basalts at the Hellisheidi geothermal field, Iceland. *International Journal of Greenhouse Gas Control, 9*, 24-40. (2012).

Audigane, P., Gaus, I., Pruess, K., & Xu, T.: Reactive transport modeling using TOUGHREACT for the long term CO2 storage at Sleipner, North Sea. Paper presented at the *Fourth Annual Conference on Carbon Capture and Sequestration DOE/NETL*, (2005).

Castillo Ruiz, N., McLean, K., Richardson, I., Misa, T., Ferguson, A., Altar, D., & Kaya, E.: Passive NCG reinjection at Te Huka geothermal binary power plant. Paper presented at the *43rd New Zealand Geothermal Workshop*, Wellington, New Zealand. (2022).

Clearwater, E., Seastres Jr, J., Newson, J., & Mulusa, G.: Modelling of scaling in a Tauhara production well. Paper presented at the *World Geothermal Congress 2015*, Melbourne, Australia. (2015).

Croucher, A. E.: PyTOUGH: A python scripting library for automating TOUGH2 simulations. Paper presented at the *New Zealand Geothermal Workshop 2011*, Auckland, New Zealand. (2011).

Croucher, A.: Recent developments in the PyTOUGH scripting library for TOUGH2 simulations. Paper presented at the *37th New Zealand Geothermal Workshop*, Taupo, New Zealand. (2015).

Erol, S., Akın, T., Başer, A., Saraçoğlu, Ö, & Akın, S.: Fluid-CO2 injection impact in a geothermal reservoir: Evaluation with 3-D reactive transport modeling. *Geothermics, 98*, 102271. (2022).

Forrest, A., Kelley, K. A., & Schilling, J.: *Selenium, tellurium and sulfur variations in basalts along the Reykjanes ridge and extension over Iceland, from 50 N to 65 N*. Palisades, NY: Interdisciplinary Earth Data Alliance (IEDA). (2017).

Gislason, S. R., & Eugster, H. P.: Meteoric water-basalt interactions. II: A field study in N.E. Iceland. *Geochimica Et Cosmochimica Acta, 51*(10), 2841-2855. (1987).

Gislason, S. R., & Oelkers, E. H.: Mechanism, rates, and consequences of basaltic glass dissolution: II. an experimental study of the dissolution rates of basaltic glass as a function of pH and temperature. *Geochimica Et Cosmochimica Acta, 67*(20), 3817-3832. (2003).

Horiuti, J.: 35 A theorem on the relation between rate constants and equilibrium constant. Paper presented at the *International Congress on Catalysis*, Philadelphia, Pennsylvania. *, 9* 339-342. (1957).

Johnson, J. W., Oelkers, E. H., & Helgeson, H. C.: SUPCRT92: A software package for calculating the standard molal thermodynamic properties of minerals, gases, aqueous species, and reactions from 1 to 5000 bar and 0 to 1000°C. *Computers & Geosciences, 18*(7), 899-947. (1992).

Knauss, K. G., Johnson, J. W., & Steefel, C. I.: Evaluation of the impact of CO2, co-contaminant gas, aqueous fluid and reservoir rock interactions on the geologic sequestration of CO2. *Chemical Geology, 217*(3), 339-350. (2005).

Kovac, K. M., Xu, T., Pruess, K., & Adams, M. C.: Reactive chemical flow modeling applied to injection in the Coso EGS experiment. Paper presented at the *31st Workshop on Geothermal Reservoir Engineering*, Stanford University, Stanford, California. (2006).

Lasaga, A. C.: Chemical kinetics of water-rock interactions. *Journal of Geophysical Research: Solid Earth, 89*(B6), 4009-4025. (1984).

Lasaga, A. C.: *Kinetic theory in the earth sciences*. Princeton, New Jersey: Princeton University Press. (1998).

Lasaga, A. C.: Fundamental approaches in describing mineral dissolution and precipitation rates. In A. F. White, & S. L. Brantley (Eds.), *Chemical weathering rates of silicate minerals* (pp. 23-86). Berlin, Boston: De Gruyter. (2018).

Leturcq, G., Berger, G., Advocat, T., & Vernaz, E.: Initial and long-term dissolution rates of aluminosilicate glasses enriched with ti, zr and nd. *Chemical Geology, 160*(1), 39-62. (1999).

Nagy, K. L., Blum, A. E., & Lasaga, A. C.: Dissolution and precipitation kinetics of kaolinite at 80 degrees C and pH 3; the dependence on solution saturation state. *American Journal of Science, 291*(7), 649-686. (1991).

Nagy, K. L., Steefel, C. I., Blum, A. E., & Lasaga, A. C.: Dissolution and precipitation kinetics of kaolinite: Initial results at 80 C with application to porosity evolution in a sandstone. In I. D. Meshri, & P. J. Ortoleva (Eds.), *M 49: Prediction of reservoir quality through chemical modeling* (pp. 85-101) American Association of Petroleum Geologists. (1990).

Nagy, K. L., & Lasaga, A. C.: Simultaneous precipitation kinetics of kaolinite and gibbsite at 80 C and pH 3. *Geochimica Et Cosmochimica Acta, 57*(17), 4329-4335. (1993).

Oelkers, E. H., & Gislason, S. R.: The mechanism, rates and consequences of basaltic glass dissolution: I. an experimental study of the dissolution rates of basaltic glass as a function of aqueous al, Si and oxalic acid concentration at 25°C and pH = 3 and 11. *Geochimica Et Cosmochimica Acta, 65*(21), 3671-3681. (2001).

Palandri, J. L., & Kharaka, Y. K.: *A compilation of rate parameters of water-mineral interaction kinetics for*

application to geochemical modeling. Menlo Park, California. (2004).

Passarella, M.: Basalt - fluid interactions at subcritical and supercritical conditions: An experimental study, *PhD Thesis, School of Geography, Environment and Earth Sciences,* Victoria University of Wellington, New Zealand. (2021).

Passarella, M., Mountain, B. W., & Seward, T. M.: Experimental simulations of basalt-fluid interaction at supercritical hydrothermal condition (400°C – 500bar). *Procedia Earth and Planetary Science, 17*, 770-773. (2017).

Passarella, M., Seward, T. M., & Mountain, B. W.: *Experimental studies of basalt-fluid interactions at subcritical and supercritical hydrothermal conditions.* Victoria University of Wellington, New Zealand. (2015).

Paul, A.: Chemical durability of glasses; a thermodynamic approach. *Journal of Materials Science., 12*, 2246-2268. (1977).

Peate, D. W., Baker, J. A., Jakobsson, S. P., Waight, T. E., Kent, A. J., R., Grassineau, N. V., & Skovgaard, A. C.: Historic magmatism on the Reykjanes Peninsula, Iceland: A snap-shot of melt generation at a ridge segment. *Contributions to Mineralogy and Petrology, 157*(3), 359-382. (2009).

Saldana, A. G. M., Kaya, E., Zarrouk, S. J., Callos, V., & Mountain, B. W.: Numerical simulation of mixed brine-CO2/H2S-rock interaction during the reinjection of non-condensable gases. Paper presented at the *41st Workshop on Geothermal Reservoir Engineering,* Stanford, California, USA. (2016).

Seol, Y., & Lee, K.: Application of TOUGHREACT to performance evaluations of geothermal heat pump systems. *Geosciences Journal, 11*(1), 83-91. (2007).

Sonnenthal, E., Ito, A., Spycher, N., Yui, M., Apps, J., Sugita, Y., . . . Kawakami, S.: Approaches to modeling coupled thermal, hydrological, and chemical processes in the drift scale heater test at Yucca Mountain. *International Journal of Rock Mechanics and Mining Sciences, 42*(5), 698-719. (2005).

Sonnenthal, E., & Spycher, N.: *Drift-scale coupled processes (DST and THC seepage) models.* United States. (2001).

Techer, I., Advocat, T., Lancelot, J., & Liotard, J.: Dissolution kinetics of basaltic glasses: Control by solution chemistry and protective effect of the alteration film. *Chemical Geology, 176*(1), 235-263. (2001).

Thorstenson, D. C., & Plummer, L. N.: Equilibrium criteria for two-component solids reacting with fixed composition in an aqueous phase; example, the magnesian calcites. *American Journal of Science, 277*(9), 1203-1223. (1977).

Wellmann, J. F., Croucher, A., & Regenauer-Lieb, K.:. Python scripting libraries for subsurface fluid and heat flow simulations with TOUGH2 and SHEMAT. *Computers & Geosciences, 43*, 197-206.

Wellmann, J. F., Finsterle, S., & Croucher, A.: Integrating structural geological data into the inverse modelling framework of iTOUGH2. *Computers & Geosciences, 65*, 95-109. (2014).

White, A. F., & Brantley, S. L.: The effect of time on the weathering of silicate minerals: Why do weathering rates differ in the laboratory and field? *Chemical Geology, 202*(3), 479-506. (2003).

White, A. F., & Peterson, M. L.: Role of reactive-surface-area characterisation in geochemical kinetic models. In D. C. Melchior, & R. L. Bassett (Eds.), *Chemical modeling of aqueous systems II* (pp. 461-475) ACS Publications. (1990).

Williams, M. D., Vermeul, V. R., Reimus, P. W., Newell, D., & Watson, T. B.: *Development of models to simulate tracer behavior in enhanced geothermal systems.* Richland, WA, United States. (2010).

Xu, T., Apps, J. A., & Pruess, K.: Mineral sequestration of carbon dioxide in a sandstone–shale system. *Chemical Geology, 217*(3-4), 295-318. (2005).

Xu, T., Apps, J. A., Pruess, K., & Yamamoto, H.: Numerical modeling of injection and mineral trapping of CO2 with H2S and SO2 in a sandstone formation. *Chemical Geology, 242*(3-4), 319-346. (2007).

Xu, T., Ontoy, Y., Molling, P., Spycher, N., Parini, M., & Pruess, K.: Reactive transport modeling of injection well scaling and acidising at Tiwi field, Philippines. *Geothermics, 33*(4), 477-491. (2004).

Xu, T., Sonnenthal, E., & Bodvarsson, G.: A reaction-transport model for calcite precipitation and evaluation of infiltration fluxes in unsaturated fractured rock. *Journal of Contaminant Hydrology, 64*(1-2), 113-127. (2003).

Xu, T., Sonnenthal, E., Spycher, N., & Zheng, L.: *TOUGHREACT V3.0-OMP reference manual: A parallel simulation program for non-isothermal multiphase geochemical reactive transport.* Berkeley, CA, USA. (2014).

Yang, L., & Steefel, C. I.: Kaolinite dissolution and precipitation kinetics at 22°C and pH 4. *Geochimica Et Cosmochimica Acta, 72*(1), 99-116. (2008).

Zimmer, K., Zhang, Y., Lu, P., Chen, Y., Zhang, G., Dalkilic, M., & Zhu, C.: SUPCRTBL: A revised and extended thermodynamic dataset and software package of SUPCRT92. *Computers & Geosciences, 90*(Part A), 97-111. (2016).

ISSN 2703-4275